Supporting Information

Boosting Initial Coulombic Efficiency in Cobalt-Free Li-Rich Layered Oxides via Facile Gas-Solid Interface Modification

Yuting Yan[a], Wei Liu[a], Hailong Wang[a], Qianjin Xiong[a], Zhimeng Liu[*b], Xin He[*a,b]

[a] *School of Chemical Engineering, Sichuan University, Chengdu 610065, China*

[b] *College of Electrical Engineering, Sichuan University, Chengdu 610065, China*

[*]Corresponding author.

E-mail address: zhimengliu@scu.edu.cn, xinhe@scu.edu.cn

Experiment

1. Material synthesis

Synthesis: The precursor was prepared using the sol-gel method. Specifically, 0.01 mol of $Ni(CH_3COO)_2 \cdot 4H_2O$, 0.03 mol of $Mn(CH_3COO)_2 \cdot 4H_2O$, 0.063 mol of $LiCH_3COO \cdot 2H_2O$ (with a 5 wt% excess), and 0.04 mol of citric acid (as a complexing agent) were dissolved in 20 mL of deionized water. After the solution became completely clear, ammonia water was added dropwise to adjust the pH to 7, followed by the addition of ethylene glycol. The resulting mixture was continuously stirred and evaporated in an oil bath at 110 °C for over 12 hours to form a gel. The gel was then dried under vacuum at 120 °C for more than 12 hours to obtain a xerogel. The xerogel was ground into a fine powder using a mortar and pestle, and the powder was calcined in a muffle furnace. The calcination process involved heating at a rate of 5 °C min^{-1} to 450 °C for 4 hours, followed by further calcination at 850 °C for 12 hours, yielding the pristine cobalt-free lithium-rich material ($Li_{1.2}Mn_{0.6}Ni_{0.2}O_2$), denoted as PR.

Gas-solid interface modification: Ammonium niobium oxalate hydrate ($C_4H_4NNbO_9 \cdot nH_2O$) was mixed with PR in a x(x=2,4,7) wt% ratio, and the mixture was calcined in a tube furnace under an argon atmosphere at 600 °C for 3 hours. Subsequently, the product was washed with water, filtered, and dried repeatedly. The material was then calcined in air at 300 °C for 3 hours, and the resulting sample was labeled as GS-x.

2. Materials characterization

Powder X-ray diffraction (XRD) patterns were acquired using a DX-2800 diffractometer (Cu Kα radiation, λ = 1.54051 Å) operating at 40 kV and 40 mA, with angular scanning performed in 0.01° increments across the 10°-90° 2θ range. Rietveld refinement of XRD data was executed through GSAS/EXPGUI software suite. In situ XRD analysis during the initial charge-discharge cycle of GS-4 samples was conducted at the CRG LISA-BM08 beamline (ESRF, France). Surface chemical states were examined by X-ray photoelectron spectroscopy (Thermo Scientific K-Alpha) while molecular structure characterization employed Raman spectroscopy (RENISHAW

system, 532 nm excitation laser). Morphological evaluation was performed using field emission scanning electron microscopy (ZEISS GeminiSEM 300-71-10), with high-resolution transmission electron microscopy and elemental mapping achieved through Talos F200X G2 equipped with EDS. Synchrotron-based soft X-ray absorption spectroscopy (s-XAS) measurements were carried out under two configurations: O *K*-edge analysis in total electron yield (TEY) and total fluorescence yield (TFY) modes at BL02B02 beamline (SSRF, China), while Ni/Mn *L*-edge studies utilized TEY mode at MCD-A/B beamlines (NSRL, Soochow Beamline for Energy Materials). For transition metal *K*-edge analysis, X-ray absorption near-edge structure (XANES) and extended X-ray absorption fine structure (EXAFS) spectra were collected in transmission mode using a laboratory XAS spectrometer equipped with Si (110), Si (533), and Si (551) spherical bent crystal analyzers (500 mm curvature radius). Spectral processing and modeling were implemented through Athena/Artemis software packages.

3. Electrochemical measurements

CR2032 coin cells were assembled with lithium metal counter electrodes in an argon-filled glovebox (H_2O/O_2 < 0.01 ppm). Cathodes were fabricated by blade-coating homogeneous slurry containing active material (80 wt%), Super P carbon (10 wt%), and PVDF binder (10 wt%) dispersed in NMP solvent onto aluminum current collectors, followed by vacuum drying at 120 °C for 12 h. The resulting electrodes (Φ12 mm) exhibited active material loadings of ~2 mg cm^{-2} and were calendared to 40 μm thickness. Electrochemical cells employed 1 M $LiPF_6$ in EC/DEC (1:1 w/w) electrolyte with Whatman glass fiber separators. Full-cells were constructed using commercial graphite as the anode, with a designed negative-to-positive (N/P) capacity ratio of 1.1. All the electrochemical performance tests were conducted using a NEWARE Battery Test System (MIHW-200-160CH, Shenzhen, China).

Galvanostatic cycling tests were performed on Neware test sysytems (MIHW-200-160CH-B). The routine cycling performance of both full-cells and half-cells was evaluated at 30°C within a voltage range of 2.0-4.8 V (vs. Li^+/Li). Three formation cycles were performed at the current of 0.1C (1C = 250 mAh g^{-1}). The low-temperature

testing protocol was as follows: cycling at 0.1C in a 0 °C environment; for the -20 °C tests, the cells were initially activated with three cycles at room temperature, then transferred to a -20 °C environmental chamber for cycling at a rate of 0.33C. Low-temperature batteries use specially formulated low-temperature electrolytes. Electrochemical impedance spectroscopy (EIS) measurements (0.01 Hz-100 kHz, 5 mV amplitude) were acquired using a Metrohm VIONIC workstation after 8 h open-circuit stabilization. Post-cycling characterization involved identical EIS protocols without disassembly. GITT profiles were obtained through intermittent current pulses (0.2C,15 min) followed by 1 h relaxation periods. For analysis, cycled cells were disassembled in glovebox, rinsed with DMC solvent, and vacuum-dried at 80 °C.

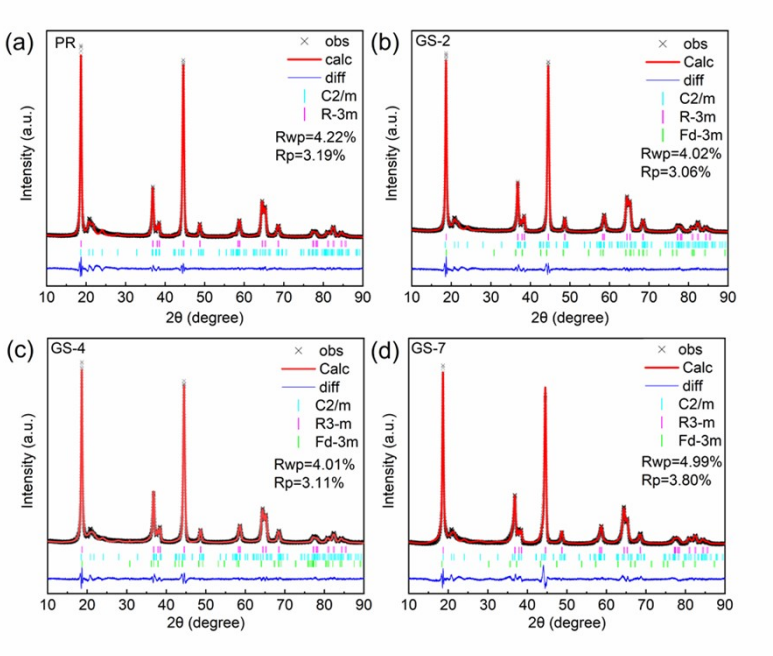

Fig. S1. Rietveld refinements of the (a) PR, (b) GS-2, (c) GS-4, (d) GS-7.

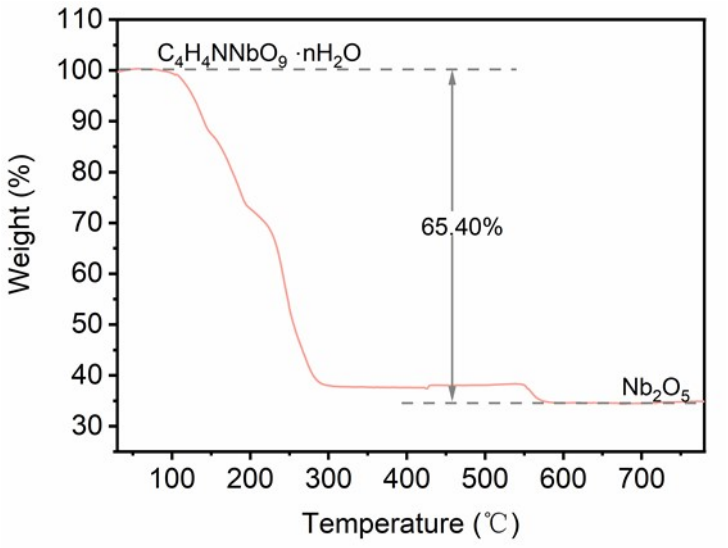

Fig. S2. The thermogravimetry measurement of $C_4H_4NNbO_9 \cdot nH_2O$.

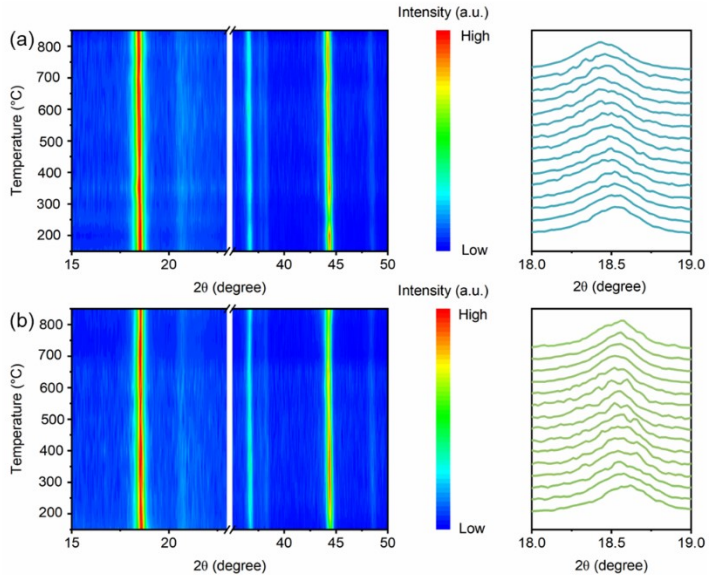

Fig. S3. In-situ variable-temperature XRD patterns of (a) PR and (b) the mixture containing PR mixed with $C_4H_4NNbO_9 \cdot nH_2O$.

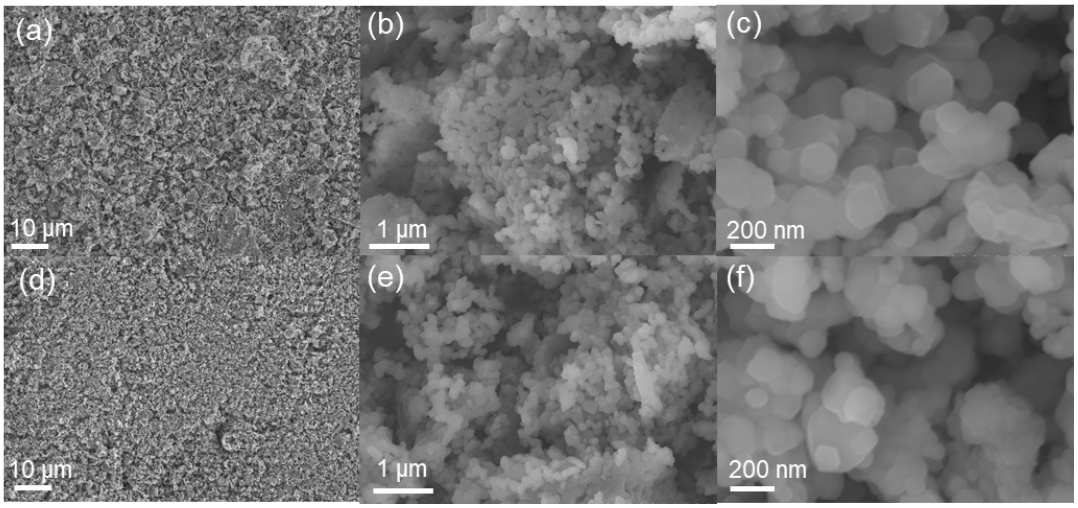

Fig. S4. SEM images of PR (a-c), GS-4 (d-f) at different magnification.

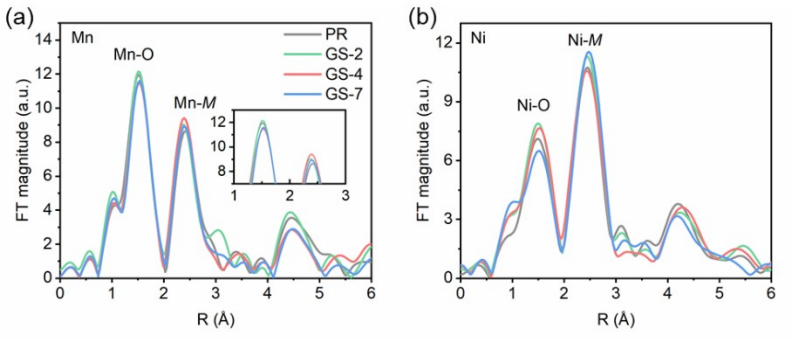

Fig. S5. the corresponding Fourier transformed magnitude of κ^3-weighted *K*-edge EXAFS of (a) Mn and (b) Ni for PR, GS-2, GS-4, and GS-7.

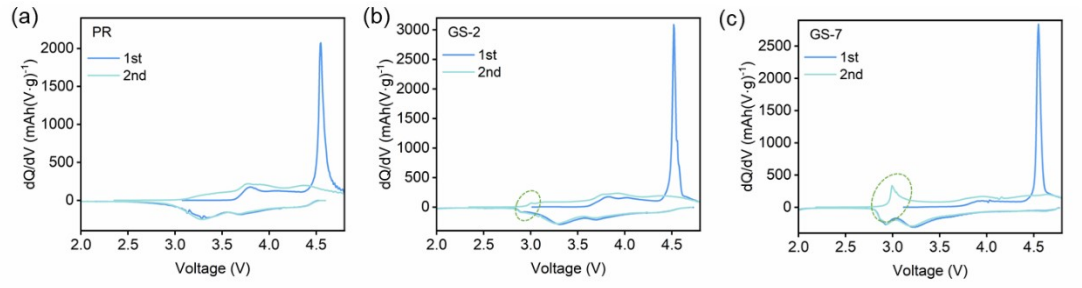

Fig. S6. The dQ/dV curves for the initial two cycles of (a) PR, (b) GS-2 and (c) GS-7.

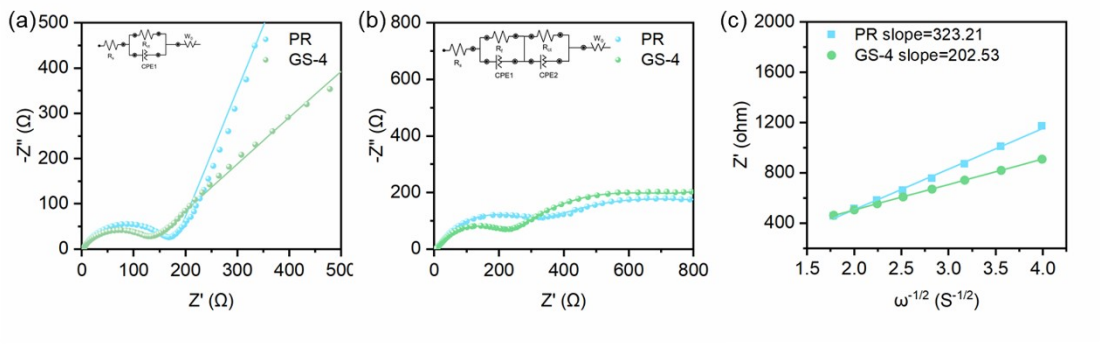

Fig. S7. Nyquist plots of PR and GS-4 (a) before cycle (b) after 200 cycles at 1C (inset: the equivalent circuit model). (c) The profiles of Z' *vs.* $\omega^{-1/2}$ from 0.1 Hz to 0.01 Hz for PR and GS-4.

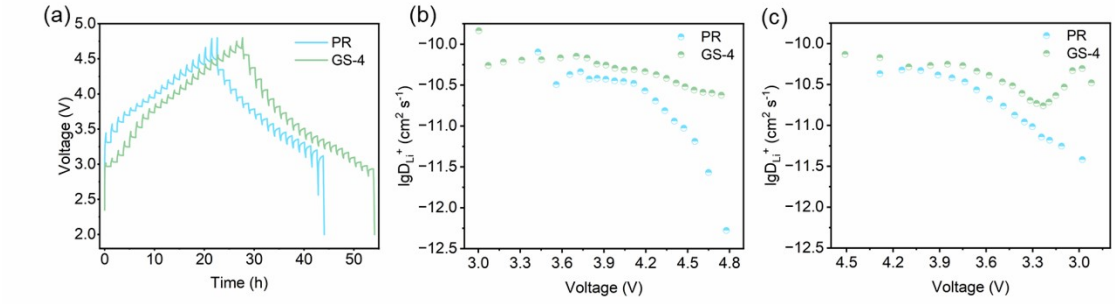

Fig. S8. (a) GITT curves at 0.2C in the second cycle; (b, c) Li^+ diffusion coefficient in different states calculated according to GITT results.

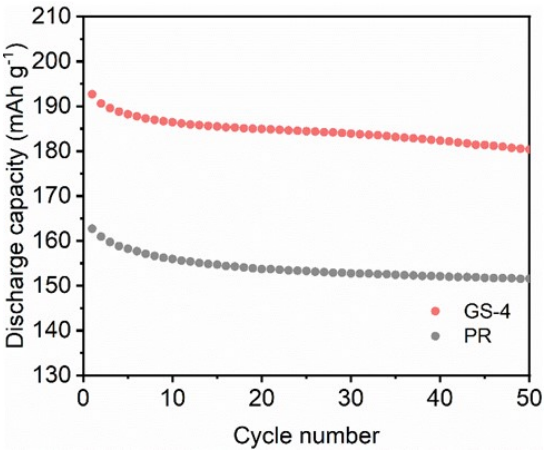

Fig S9. The full-cell cycling performance of GS-4 and PR.

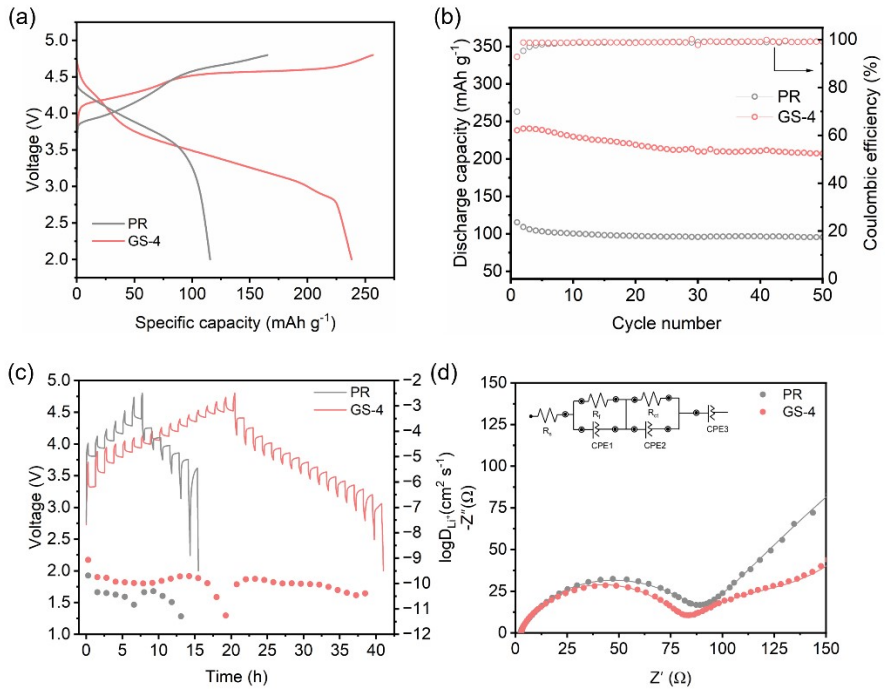

Fig. S10. (a) Initial charge-discharge profiles and (b) Cycle performance of PR and GS-4 between 2.0 and 4.8 V at 0 °C and 0.1C. (c) GITT curves and calculated lithium ion diffusion coefficients of PR and GS-4. (d)Nyquist plots of PR and GS-4 after cycles at 0.1C and 0 ℃ (inset: the equivalent circuit model).

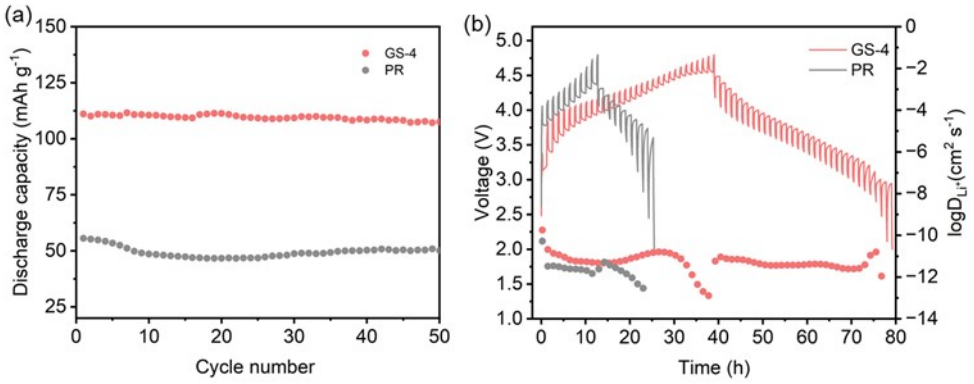

Fig S11. (a) Cycle performance of PR and GS-4 between 2.0 and 4.8 V at -20 °C and 0.33C. (b) GITT curves and calculated lithium ion diffusion coefficients of PR and GS-4, measured at 0.1C rate.

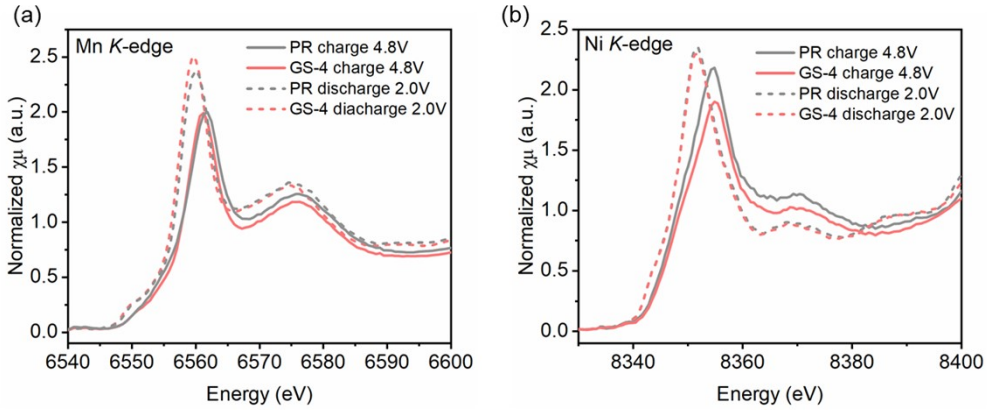

Fig. S12. Normalized ex situ XANES spectra at (a) Mn *K*-edge and (b) Ni *K*-edge of PR and GS-4 at various charge-discharge states during the first cycle.

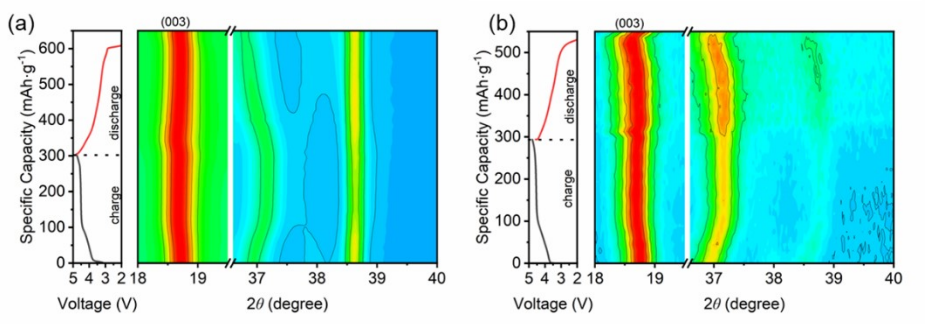

Fig. S13. In-situ XRD results of (a) GS-4 and (b) PR during the initial cycle in the voltage range of 4.8-2.0 V using a current rate of 0.1C.

Table S1. Rietveld refinements results of PR, GS-2, GS-4 and GS-7.

		Samples	PR	GS-2	GS-4	GS-7
Lattice parameters	R3-m	a=b (Å)	2.8580	2.8633	2.8628	2.8599
		c (Å)	14.2228	14.2503	14.2637	14.2506
		c/a	4.9765	4.9769	4.9824	4.9829
		Volume ($Å^3$)	100.608	101.181	101.242	100.942
	C2/m	a (Å)	4.9645	4.9541	4.9977	5.0356
		b (Å)	8.5695	8.5420	8.5564	8.5502
		c (Å)	5.0688	5.0967	5.0894	5.0325
		Volume ($Å^3$)	202.855	203.020	205.182	204.417
	Fd-3m	a =b = c(Å)	/	8.2162	8.2276	9.0835
Phase fraction (wt.%)	R3-m		51.238	62.044	66.020	66.199
	C2/m		48.762	37.901	33.920	32.958
	Fd-3m		/	0. 551	0.597	0.843

Table S2. Comparison of ICE performance of lithium-rich manganese-based batteries reported in the literature. All data are obtained from half-cell tests.

Samples	Co Status	ICE	Rate	Discharge Capacity (mAh/g)	Ref
LRMO-Gly2	Y	97.1%	0.1C	284.7	[1]
LRMO-Gly3	Y	102.5%	0.1C	258.3	[1]
OAT-3	Y	97%	0.2C	296	[2]
OAT-5	Y	100.7%	0.2C	283	[2]
B3	Y	91.5%	20 mAh/g	289	[3]
2-BNF-LLO	Y	90.29%	0.1C	~280	[4]
W2	Y	97.62%	0.1C	~275	[5]
W3	Y	107.42%	0.1C	~235	[5]
0.01F-Sur	N	85.12%	0.1C	274	[6]
NM-2	N	83.2%	0.1C	280.5	[7]
LRO-RA	N	79%	0.1C	~295	[8]
LMR-C-SPS	N	71.8%	0.1C	319.4	[9]
0.7TF-LRNMO	N	80.43%	0.1C	220.7	[10]
GS-2	N	93.9%	0.1C	294.8	This work
GS-4	N	100.4%	0.1C	306.5	This work
GS-7	N	108.7%	0.1C	292.7	This work

Table S3. Impedance Parameters of all samples before cycle.

Sample	R_s （Ω）	R_{ct}（Ω）	$D_{Li+}(cm^2s^{-1})$
PR	3.02	172.77	1.11500×10^{-10}
GS-4	3.05	118.17	3.72833×10^{-10}

Table S4. Impedance Parameters of all samples after cycle.

Sample	R_s （Ω）	R_f（Ω）	R_{ct}（Ω）
PR	3.89	242	431
GS-4	3.68	174	333

Table S5. Impedance Parameters of all samples after cycle at 0 °C.

Sample	R_s （Ω）	R_f（Ω）	R_{ct}（Ω）
PR	2.31	84.1	705
GS-4	2.65	76.3	60.8

Reference:

1 T. Zeng, Z. Jiao, X. Gao, M. Yang, X. Wang, W. Zhao, W. Tang, M. Chu, Z. He, J. Li, Z. Huang, G. Chen, Z. Chen, R. Wang, L. Wang, J. Zhang, L. He, Y. Pu and Y. Xiao, *Angew.*

Chemie - Int. Ed., 2025, **64**, e202501777.

2 W. Guo, C. Zhang, Y. Zhang, L. Lin, W. He, Q. Xie, B. Sa, L. Wang and D. L. Peng, *Adv. Mater.*, 2021, **33**, 2103173.

3 D. Fu, X. Zhang, Y. Zhou, K. Yang, J. Fan, L. Li and C. Fu, *ACS Sustain. Chem. Eng.*, 2025, **13**, 3311–3320.

4 Z. Su, Z. Guo, H. Xie, M. Qu, G. Peng and H. Wang, *ACS Appl. Mater. Interfaces*, 2024, **16**, 39447–39459.

5 X. Gao, S. Zhang, J. Guo, H. Zhang, S. Li and Z. Zhang, *J. Colloid Interface Sci.*, 2024, **663**, 601–608.

6 W. Li, J. Dong, Y. Zhao, J. Zhao, H. Wang, N. Li, Y. Lu, J. Hao, Y. Wu, Y. Fang, Y. Li, Q. Qi, Y. Su, F. Wu and L. Chen, *J. Colloid Interface Sci.*, 2024, **675**, 251–262.

7 G. guo Cui, P. Yang, P. yao Li, Y. J. Chen, J. feng Zhang, X. hui Zhang and J. chao Zheng, *J. Energy Storage*, 2025, **131**, 117549.

8 M. Yang, T. Zeng, D. He, Z. Jiao, S. Chen, W. Zhao, Y. Li, Z. Chen, Y. Pu, Y. Mu, Z. He, X. Gao, M. Chu, W. Ji, L. Cao, J. Xu, W. Yin, R. Wang and Y. Xiao, *Small*, 2025, **21**, 2502469.

9 X. Gao, G. Chen, W. Yao, Y. Mu, L. Hu, T. Zeng, W. Zhao, Z. Huang, M. Yang, Y. Pu, W. Ji, Z. Tan, P. Miao, N. Zhang, L. Yu, L. Zeng, R. Wang and Y. Xiao, *Energy Storage Mater.*, 2025, **76**, 104104.

10 Z. Li, W. Song, D. Zhang, Q. Wang, H. Sun, Q. Sun and B. Wang, *ACS Appl. Mater. Interfaces*, 2024, **16**, 25210–25220.